

Local coordination environment triggers key Ni-O-Si copolymerization on silicalite-2 for dry reforming of methane

Yidan Zhang^a, Shuqing Li^{b,*}, Yu Fu^b, Lei Zheng^b, Hongyu Li^c, Wenbo Kong^b, Bingrong Pan^b, Jiong Li^d, Jun Zhang^{b,c,e,**}, Yuhua Sun^{a,*}

^a School of Physical Science and Technology, ShanghaiTech University, Shanghai 201210, People's Republic of China

^b CAS Key Laboratory of Low-Carbon Conversion Science and Engineering, Shanghai Advanced Research Institute, Chinese Academy of Sciences, Shanghai 201210, People's Republic of China

^c Gaolu Air Products and chemicals (Shanghai) Energy Technology Co., Ltd, Shanghai 201620, People's Republic of China

^d Shanghai Synchrotron Radiation Facility, Shanghai Advanced Research Institute, Chinese Academy of Science, Shanghai 201210, People's Republic of China

^e University of the Chinese Academy of Sciences, Beijing 100049, People's Republic of China

ARTICLE INFO

Keywords:

Heterocatalysis
Local coordination environment
Dry reforming of methane
Grafted Ni(II) intermediates
Ni-O-Si copolymerization

ABSTRACT

The development of dry reforming of methane (DRM) catalysts with good Ni loading, while retaining high metal dispersion is a critical issue, given the harsh industrial-relevant conditions. Here, we demonstrate the impact of the local coordination environment on the DRM activity of Ni-silicalite-2 (Ni-S2) catalysts. The grafted Ni(II) intermediates with high Ni-O-Si copolymerization (coordination number ratio Si: Ni=2.28) are discovered to redisperse Ni sites, even at 10 wt% Ni loading. Then, the partial S2 recrystallizes into new SiO₂-nanowires to anchor Ni nanoparticles, via an ethylenediamine-assisted dissolution-recrystallization (enDR). Compared to the typical Ni-S2 catalyst with Ni phyllosilicate (CN ratio Si: Ni < 1), the Ni-S2-enDR shows high dispersion and stability at 800 °C and 450 L g_{cat}⁻¹ h⁻¹, exhibiting negligible coke deposition and no growth of 4.25 nm Ni nanoparticles. The atomic level insights in nickel and silicon coordination reported in this work provide an instructive way of designing stable DRM catalysts.

1. Introduction

Over the last few years, extreme weather and natural disasters have driven the effort to reduce and utilize the carbon dioxide produced from fossil fuels [1]. The production of each ton of steel has emitted 1.7–1.8 tons of carbon dioxide, which has led to a total CO₂ emission exceeding 1.8 billion tons since 2020 [2,3]. Dry reforming of methane (DRM) is a feasible process for the direct conversion of CO₂ with methane (coalbed, biogas, etc.) into syngas with low H₂/CO ratios [4,5]. Thus, DRM reaction is playing an increasing role in the integration of sustainable development, in view of its distinctive role to serve as a bridge connecting industrial exhausted gas and the production of environmental-friendly chemicals [6–8].

In the DRM process, the surface energy of the metal adsorbents and the Gibbs free energy of the elementary reactions are two important factors for the catalytic activity. The order of metal activity for DRM was

calculated as Rh ≈ Ir ≈ Ni > Pt ≈ Cu ≈ Pd > Au ≈ Ag [9]. The adsorption surface energy for CH₄ on Rh, Ir and Ni and their intermediates were relatively low, leading to strong adsorption affinity [9,10]. As a result, these metals exhibited high catalytic DRM activity. Moreover, considering the cost, Ni-based catalysts are promising for industrial applications [11]. However, a high number of adsorbed carbon atoms (C*) results in aggregation at grain boundaries or steps due to the high solubility of C* in nickel lattice [12]. Subsequently, the C* species will accelerate nucleation and growth into non-activated carbon. On the other hand, the increase in the number of C* decreases the activation energy of graphite carbon species at the bulk phase, while increasing the activation energy of graphite carbon species at the edge of metal particles [13,14]. As a result, the Ni surface is more susceptible to carbon deposition. Moreover, Ni-based catalysts are accompanied by the challenge of sintering due to metal particle migration and aggregation, or Ostwald ripening at high reaction temperatures [15,16]. Confining Ni

* Corresponding authors.

** Corresponding author at: CAS Key Laboratory of Low-Carbon Conversion Science and Engineering, Shanghai Advanced Research Institute, Chinese Academy of Sciences, Shanghai 201210, People's Republic of China.

E-mail addresses: lisq@sari.ac.cn (S. Li), zhangj@sari.ac.cn (J. Zhang), sunyh@sari.ac.cn (Y. Sun).

<https://doi.org/10.1016/j.apcatb.2024.123903>

Received 8 December 2023; Received in revised form 25 February 2024; Accepted 29 February 2024

Available online 2 March 2024

0926-3373/© 2024 Published by Elsevier B.V.

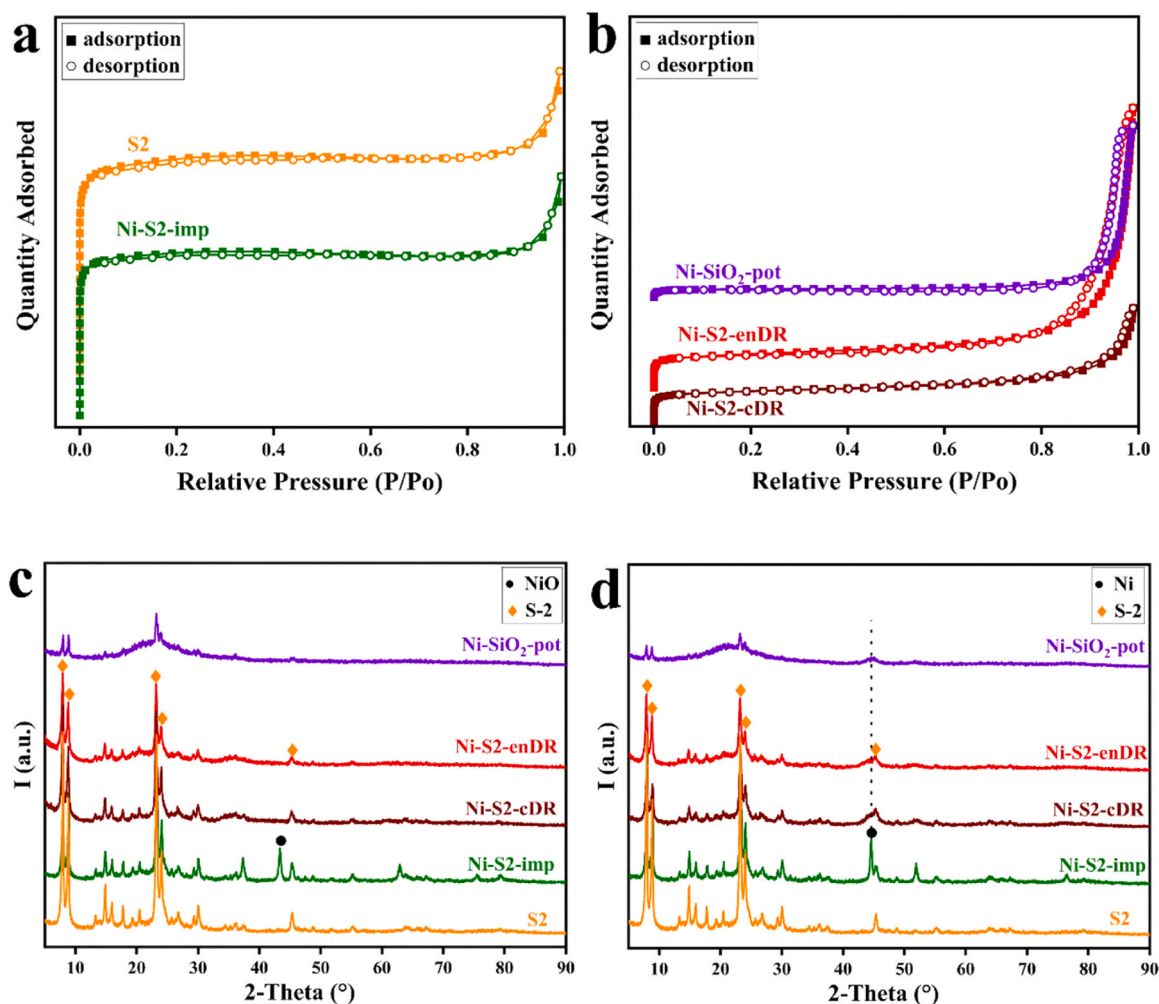


Fig. 1. a) type-I isotherms of S2 and Ni-S2-imp. b) type-IV isotherms of Ni-SiO₂-pot, Ni-S2-enDR, and Ni-S2-cDR. c) XRD patterns of the fresh samples. d) XRD patterns of the catalysts after DRM reaction.

nanoparticles (NPs) is one of the effective approaches to address these issues. The restriction of Ni NPs in pore channels [17,18], the construction of core-shell structures [19], and the employment of other composite structures were the main physical strategies [20–23]. The chemical strategies were to improve the dispersibility of Ni NPs by enhancing metal-support interaction [24], for example: solid solutions [25], alloys [26], and intermetallic carbide [27].

Recently, Kong et al. [21] reported a one-pot hydrothermal method to prepare an ultra-low loading of 0.3% Ni@S1 catalyst with a Ni size of 2.5 nm. The CH₄ conversion was 25% at 650 °C and gas hourly space velocity (GHSV) of 20 L g_{cat}⁻¹ h⁻¹ in DRM, where no carbon formation was observed. Compared to silicalite-1 (S1), the silicalite-2 (S2) zeolite was reported to be a better support for Ni-based reforming catalysts due to its vertical pore structure, which could decrease the diffusion resistance while retaining excellent thermal stability and mechanical strength [28]. Wang et al. [18] used the same one-pot method to clamp 0.3% Ni NPs between two layers of tetrahedral silica and obtained a Ni@S2 catalyst with an ultra-fine Ni size of 2.6 nm. At 650 °C and 20 L g_{cat}⁻¹ h⁻¹ in DRM, the CH₄ conversion was 48%. However, When the GHSV was increased to 100 L g_{cat}⁻¹ h⁻¹, the CH₄ conversion decreased to 17% at 650 °C in DRM. It was reported that in the industrial application of DRM, a high Ni loading was required to ensure a sufficient mass-specific reaction rate [17]. Vitale et al. increased the Ni loading on ZSM-5 zeolite to 5% by one-pot method and reported that as the amount of Ni loading increases, the textural properties of the Ni-ZSM-5 catalysts were modified and lower micropore area and volume and higher mesopore and

total volumes were observed [29]. Lu et al. [30] developed a novel two-step method to highly disperse 5% nickel in S2 zeolite. However, after a period of DRM reaction, the large nickel particle of spent Ni/S2 and coke deposition were observed. In this context, it is essential to design a perfect balance between the dispersion of Ni nanoparticles and the confinement effect at high Ni loading [31–34].

Here, we developed for the first time a highly DRM-active Ni-S2-enDR catalyst by tuning the distribution of hydroxy Ni and hydroxy Si in an ethylenediamine-assisted dissolution-recrystallization (enDR) process. Atomic-level investigations of the local coordination environment were carried out in this work, such as H₂-TPR, XPS, UV-vis, FTIR, and EXAFS, to understand the nickel-silicon coordination on Ni-S2 catalysts during dry reforming of methane. Firstly, grafted Ni(II) intermediates with a high coordination number ratio (2.28) of Si to Ni atoms were formed in the dissolution process. Then, the partial silica tetrahedra of S2 regrew into a nanowire near the grafted Ni(II) nucleus in the recrystallization process. Thus, the Ni-S2-enDR catalyst with a unique nanowire mainly consisted of silica, embedded with 4.25 nm Ni NPs at 10% Ni loading, achieves an excellent balance of high dispersion with a good Ni loading. Even under the harsh DRM reaction conditions, the Ni-S2-enDR not only exhibited excellent activity but also hindered the carbon deposition and the growth of Ni NPs due to the synergistic confinement of nanowire and pore structure. We also compared other samples, including the Ni-S2-cDR catalyst obtained by conventional dissolution-recrystallization, the Ni-S2-imp catalyst prepared via impregnation, and the Ni-SiO₂-pot catalyst synthesized through a one-

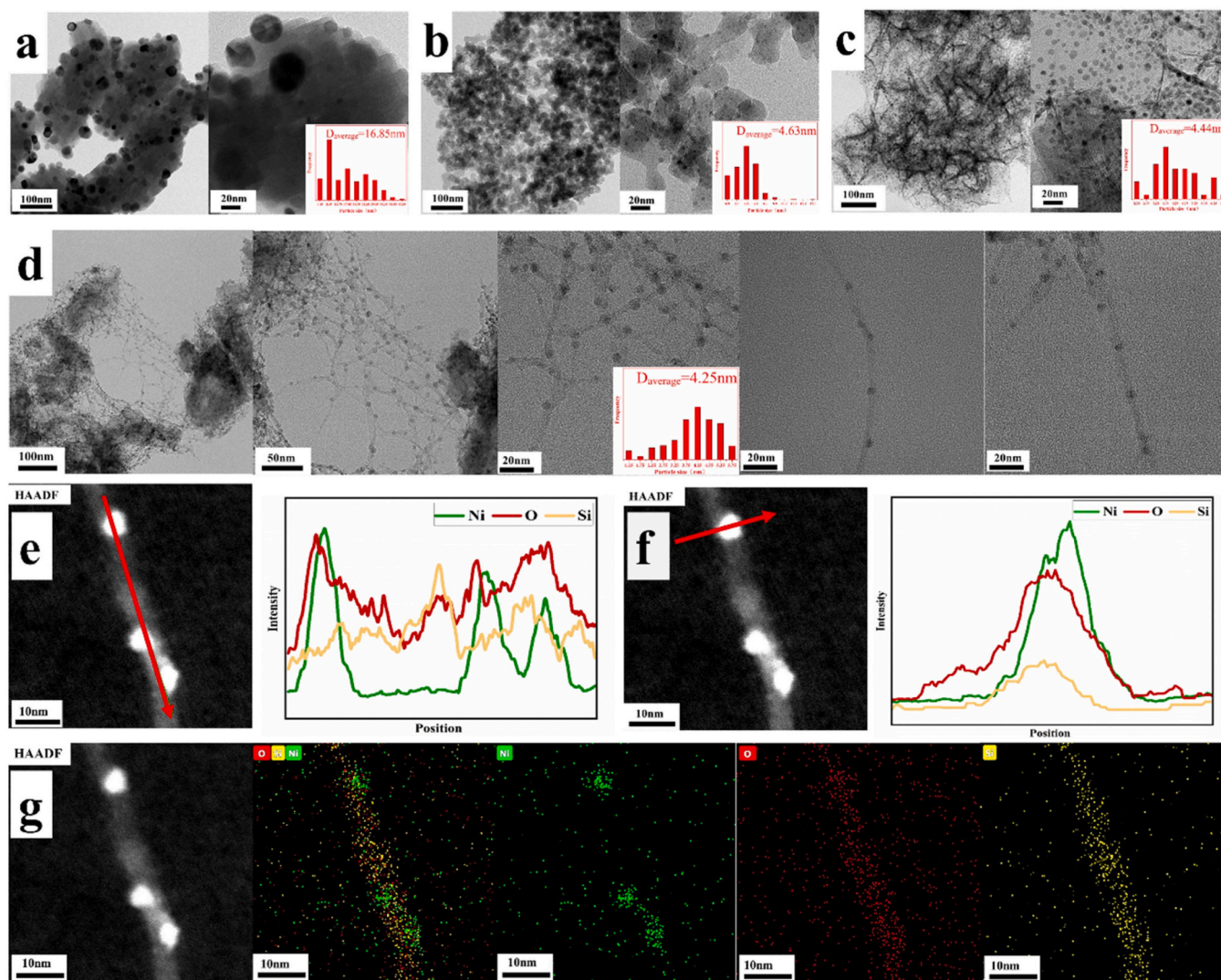


Fig. 2. TEM image of the reduced catalysts: a) Ni-S2-imp; b) Ni-SiO₂-pot; c) Ni-S2-cDR; d) Ni-S2-enDR, and STEM-HAADF image of the Ni-S2-enDR sample with EDS elemental line-scan at the e) longitudinal and f) transverse directions. g) The EDS elemental maps (O, Si, and Ni elements are labeled as red, yellow, and green, respectively).

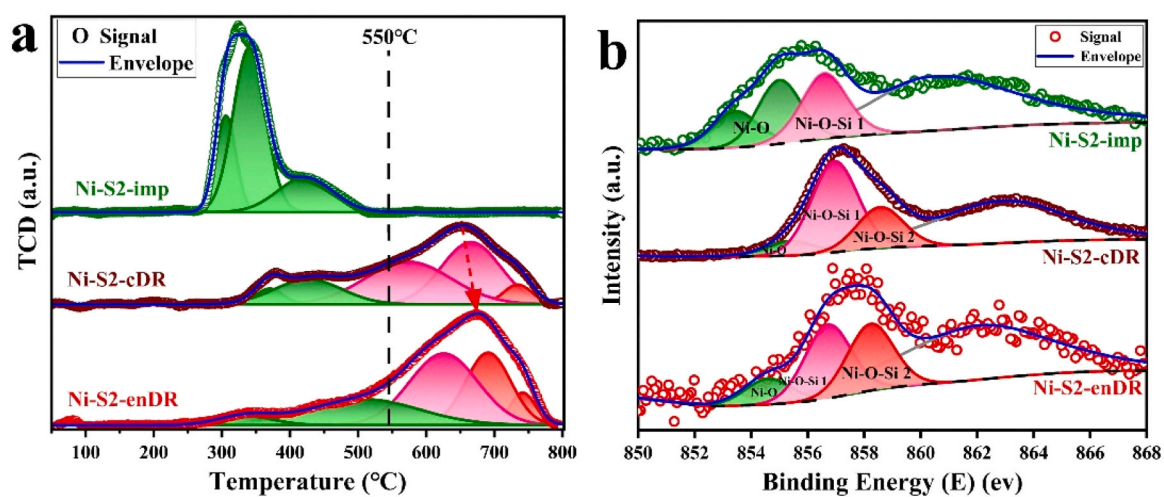


Fig. 3. a) H₂-TPR results of different catalysts. b) The Ni 2p XPS spectra of different fresh catalysts.

Table 1

The proportion of surface Ni species at corresponding Ni 2p binding energy over the fresh catalysts.

Sample	Nickel oxide		Nickel silicate			
	Ni-O		Ni-O-Si 1		Ni-O-Si 2	
	Ni 2p (eV)	Proportion (%)	Ni 2p (eV)	Proportion (%)	Ni 2p (eV)	Proportion (%)
Ni-S2-imp	853.4/855	22.37/36.56	856.6	41.07	-	-
Ni-S2-cDR	855.4	10.07	856.9	61.98	858.6	27.96
Ni-S2-enDR	854.6	15.53	856.7	44.26	858.2	40.21

pot approach.

2. Experimental section

2.1. Catalyst preparation

The chemicals used in this work were tetraethyl orthosilicate (>99%,

TEOS), tetrabutylammonium hydroxide (40 wt%, TBAOH), nickel (II) nitrate hexahydrate solid ($\text{Ni}(\text{NO}_3)_2 \cdot 6 \text{H}_2\text{O}$), ethylenediamine (>99%, EN), ethanol (>99%, EtOH). All chemicals were sourced from Sigma-Aldrich and used without any purification. Homemade deionized water (18.5 M Ω -cm) was used for the catalyst preparation.

S2 zeolite was synthesized through a conventional hydrothermal method [35,36]. Specifically, TEOS: H_2O : TBAOH in a molar ratio of 1: 12: 0.35 were mixed and stirred, until TEOS was fully hydrolyzed. In the next step, the clarified solution was heated at 170 °C in a polytetrafluoroethylene-lined autoclave for 3 days. The hydrothermal suspension was centrifuged, and the obtained solid sample was washed repeatedly with EtOH and dried overnight at 120 °C. Finally, the S2 zeolite was obtained after removing the template at 550 °C for 5 h.

The Ni-S2-enDR catalyst was synthesized through an ethylenediamine-assisted dissolution-recrystallization method. Specifically, 2 ml of nickel nitrate solution was mixed (the concentration was calculated to obtain a 10 wt% Ni loading) with 1 g of the homemade S2 sample. A mixed solid was obtained by completely evaporating the water with magnetic stirring at room temperature. In the next step, the obtained solid was mixed and dissolved by ultrasound with a mixed solution prepared with 40 ml of 0.3 M TBAOH and excessive EN. Then,

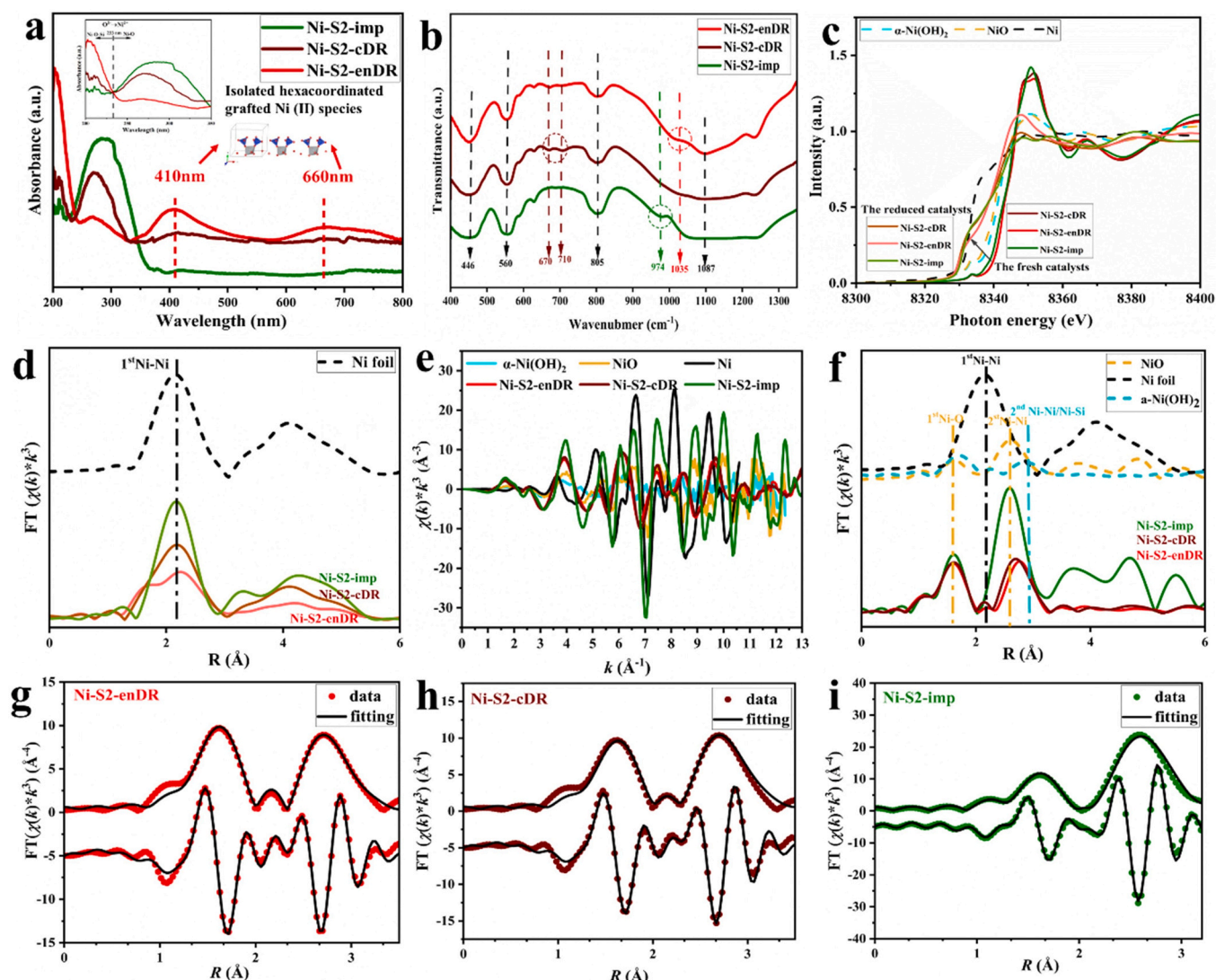


Fig. 4. a) UV-vis spectra of the fresh catalysts. b) FTIR spectra of the fresh catalysts. c) normalized Ni K-edge XANES spectra for the fresh and the reduced catalysts. d) Ni K-edge EXAFS spectra in the R-space for the reduced catalysts. Ni K-edge EXAFS spectra for the fresh catalysts and standard samples in the e) k-space and f) R-space. The data are k^3 -weighted and not phase-corrected. g-i) the curvefit (black line) and EXAFS (red points) for the fresh catalysts, shown in R-space (FT magnitude and imaginary component).

Table 2
Curve-fit Parameters* for Ni K-edge EXAFS for the fresh catalyst.

Sample	Path**	coordination number (CN)	2 nd CN ratio (Ni:Si: Ni-Ni)	distance (R)/Å	R factor
Ni-S2-imp	1st Ni-O	6.6±0.7	0	2.08±0.01	0.030
	2nd Ni-Ni	15.1±1.3		2.96±0.008	
Ni-S2-cDR	1st Ni-O	6.4±0.2	0.85	2.07±0.004	0.011
	2nd Ni-Ni	5.2±0.6		3.02±0.008	
	2nd Ni-Si	4.4±0.4		3.27±0.007	
	1st Ni-O	6.5±0.2	2.28	2.06±0.005	0.007
Ni-S2-enDR	2nd Ni-Ni	2.9±0.4		3.07±0.01	
	2nd Ni-Si	6.6±0.6		3.25±0.01	

* S_0^2 was fixed as 0.9. ΔE_0 was refined as a global fit parameter for one sample. Data ranges: $2.3 \leq k \leq 11 \text{ \AA}^{-1}$, $1 \leq R \leq 3.3 \text{ \AA}$. The variable parameters out of a total of 10.8 independent data points.

** The Ni-O and Ni-Ni paths are from the crystal structure of 4320508, NiO file in the Crystal Open Database (COD) crystal database for fitting the Ni-S2-imp sample; The Ni-O, Ni-Ni, and Ni-Si paths are from the crystal structure of $\text{Si}_2\text{Ni}_3\text{H}_4\text{O}_9$ file in the Materials Explorer (PE) crystal database for fitting the Ni-S2-cDR, Ni-S2-enDR samples.

the sol was heated at 170 °C in a polytetrafluoroethylene-lined autoclave for 1 day. Afterward, the obtainable solid was washed repeatedly with EtOH, which was then dried at 100 °C for 6 h under a vacuum. Finally, the fresh Ni-S2-enDR catalyst was obtained by removing the template at 550 °C for 5 h.

The Ni-S2-cDR catalyst was synthesized using a conventional dissolution-recrystallization method [17]. The synthesis strategy was similar to the preparation of the Ni-S2-enDR catalyst, with the difference that no EN was added to the mixed solution, and only 40 ml of 0.3 M TBAOH solution dissolved the mixed solid.

The Ni-S2-imp catalyst was prepared via wet impregnation. Specifically, 2 ml nickel nitrate solution was added to 1 g homemade S2 solid and vigorously stirred at room temperature. Followed by drying overnight at 120 °C, and the fresh Ni-S2-imp catalyst was obtained by calcining at 550 °C for 5 hours.

The Ni-SiO₂-pot catalyst was prepared via a one-pot hydrothermal method [18]. Specifically, TEOS: H₂O: TBAOH in a molar ratio of 1: 12: 0.35 were mixed and stirred at room temperature until a clear solution was obtained. Then, added nickel nitrate complexed by excessive EN with stirring for 1 h. Next, the obtained mixture was heated at 170 °C in a polytetrafluoroethylene-lined autoclave for 3 days. The subsequent washing and calcination of hydrothermal suspension was similar to the processes mentioned above.

2.2. Catalyst characterization

The Rigaku Ultima IV powder diffractometer was used for X-ray powder diffraction (XRD) characterization, with Cu K α radiation as a source of radiation ($\lambda = 0.15408 \text{ nm}$) at 40 kV and 40 mA. The diffractograms of prepared samples were compared with the standard database in Jade 6.0 software to determine the crystal structure.

The FEI Talos F200x was used for the transmission electron microscope (TEM), operated at 200 kv, while the Talos was equipped with a Super-X detector of energy dispersive spectrometer (EDS), and the HAADF images were collected by STEM mode with a high-angle annular dark field detector in the range of 37–200 mrad.

The Micromeritics ASAP 2420 physisorption analyzer was used for

nitrogen (N₂) physical adsorption-desorption experiments. Prior to tests, the samples were pretreated under vacuum at 300 °C for 10 h. Adsorption-desorption tests of the samples were performed at −196 °C. The specific surface area (S_{BET}) of the samples was calculated using the Brunauer–Emmett–Teller (BET) method, while the investigation of micro- and meso-porosity was carried out with a T-plot method.

Temperature-programmed reduction with H₂ (H₂-TPR) was performed using an Auto Chem II 2920 setup, equipped with a 5 A molecular sieve and a thermal conductivity detector (TCD). In a typical process, the 100 mg sample was loaded into a U-shaped quartz tube, and pretreated by heating to 200 °C in He for 1 h before cooling down to room temperature. Next, the baseline was stabilized in a 5% H₂/He flow, followed by heating up with a temperature ramp of 10 °C/min to 800 °C and held for 10 min. H₂-pulse chemisorption was used to determine the dispersion of metal Ni on the Auto Chem II 2920 setup. The 50 mg sample was pretreated in H₂ at 750 °C for 30 min, and cooled down to 50 °C in He to degas for 30 min. Next, H₂ was dosed on the samples every 2 min until saturation.

X-ray photoelectron spectroscopy (XPS) was performed using a Thermo Fisher Scientific ESCALAB 250Xi analyzer, with Al K α radiation as a source of radiation ($h\nu = 1486.76 \text{ eV}$). The sample chamber pressure was below $8.6 \times 10^{-7} \text{ Torr}$. The binding energy values of all samples were calibrated based on a C 1 s peak at 284.8 eV. UV–visible (UV–vis) diffuse reflectance spectroscopy was measured by using a UV2700 spectrophotometer equipped with a diffuse reflectance accessory in the range of 200–800 nm. Fourier transform Infrared absorption spectra (FTIR) was measured by using a Thermo Fisher iS10 spectrometer. Samples were mixed with KBr to form a uniform wafer. The scanning contains 32 times from 400 to 4000 cm^{−1}. X-ray absorption spectra of the catalysts at the Ni K-edge were measured at the BL11B beamline of the Shanghai Synchrotron Radiation Facility. The radiation is monochromatic by a double crystal Si (111) monochromator and focused by a rhodium-coated mirror. Extended X-ray absorption fine structure (EXAFS) data was processed, including Fourier transform (FT) by the Athena-series software to calculate the best fitting of the simulated crystal structure path by Feff6.

Thermogravimetric analysis (TGA) was performed on a STA4449F3 Jupiter thermogravimetric analyzer. The sample was pretreated by heating to 200 °C for 2 h under Ar flow, cooled down to 100 °C, switched to air at 50 cm³ STP min^{−1}, and held until baseline stabilized. The amount of carbon deposition of the spent catalysts was monitored to 900 °C at 10 °C/min.

Raman spectra was performed on a T64000 Jobin Ivon spectrometer using a 715 nm Ar ion laser and an (Electron Multiplying Charge-Coupled Device) EMCCD detector.

2.3. DRM catalytic tests

The catalytic performance of the prepared catalysts in the DRM reaction was evaluated with a single-stage adiabatic fixed-bed reactor (inner diameter of quartz tube = 8 mm). The reactor was equipped with a thermocouple located at the constant temperature region of the bed to monitor the real-time reaction temperature. The composition of outlet gas was analyzed online by an INFICON 3000 Micro gas chromatograph. The 50 mg fresh catalyst was loaded into the fixed-bed reactor and was reduced in 80 ml/min 50% H₂/N₂ flow at 750 °C for 2 h to ensure a complete reduction of Ni²⁺ to Ni⁰. For reactivity tests, all catalysts were performed under atmospheric pressure at different temperatures (500–800 °C, interval of 50 °C), with a gas flow of 150 ml/min (CH₄: CO₂: N₂ = 1:1:2). Additionally, the Ni-S2-enDR catalyst was evaluated at a different gas hourly space velocity (GHSV) in the range of 180000–450000 ml g_{cat}^{−1} h^{−1} at 750 °C. The higher space velocity was regulated by reducing the amount of catalyst used (50–20 mg). Then, the catalytic performance of prepared catalysts was compared at a high GHSV of 450000 ml g_{cat}^{−1} h^{−1} and 750 °C. For long-term stability tests, samples were exposed to a GHSV of 180000 ml g_{cat}^{−1} h^{−1} at 750 °C for

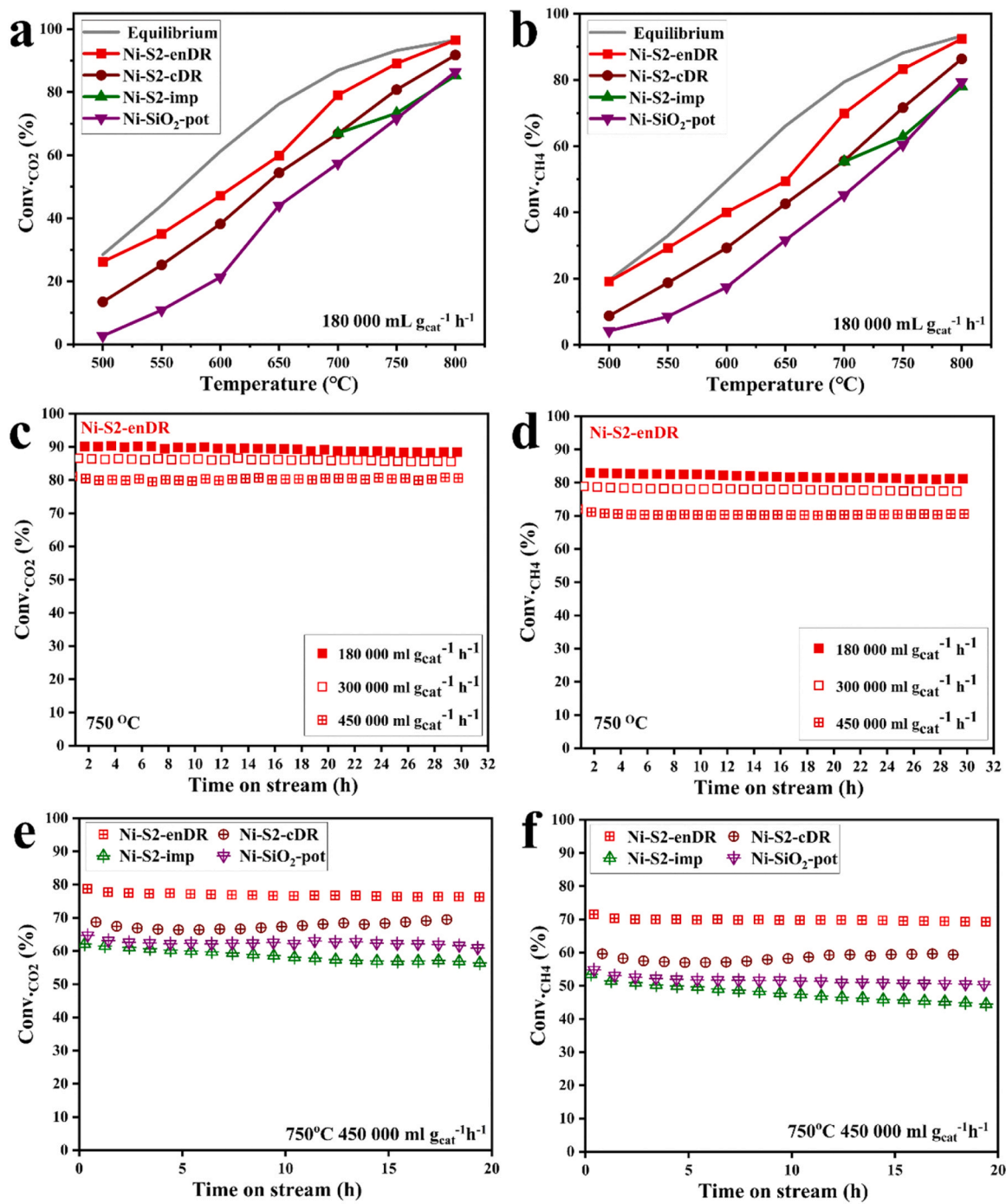


Fig. 5. a) The CO₂ conversion; b) The CH₄ conversion for different samples at different temperatures. c) The CO₂ conversion; d) The CH₄ conversion for the Ni-S2-enDR sample at different high GHSV tests. e) The CO₂ conversion; f) The CH₄ conversion of different samples for high GHSV durability tests.

40 hours. Moreover, for the coking suppression test, samples were exposed to a condition where carbon formation is thermodynamically favorable (650 °C, 180000 ml g_{cat}⁻¹ h⁻¹).

The CH₄ conversion ($Conv_{CH_4}$), CO₂ conversion ($Conv_{CO_2}$), H₂/CO molar ratio, and C balance was calculated using the following Eq. (1)–(4), respectively, to evaluate the catalytic performance of the catalyst. The carbon (C) balance of all catalysts during the long-term stability tests was in the range of 94~100%.

$$Conv_{CH_4} (\%) = \frac{F_{CH_4,in} - F_{CH_4,out}}{F_{CH_4,in}} \times 100\% \quad (1)$$

$$Conv_{CO_2} (\%) = \frac{F_{CO_2,in} - F_{CO_2,out}}{F_{CO_2,in}} \times 100\% \quad (2)$$

$$H_2 / CO = \frac{F_{H_2,out}}{F_{CO,out}} \quad (3)$$

$$C \text{ balance} (\%) = \frac{F_{CO_2,out} + F_{CH_4,out} + F_{CO,out}}{F_{CO_2,in} + F_{CH_4,in}} \quad (4)$$

Where F_{in} and F_{out} are the flow rates of corresponding gas at the inlet and outlet, respectively.

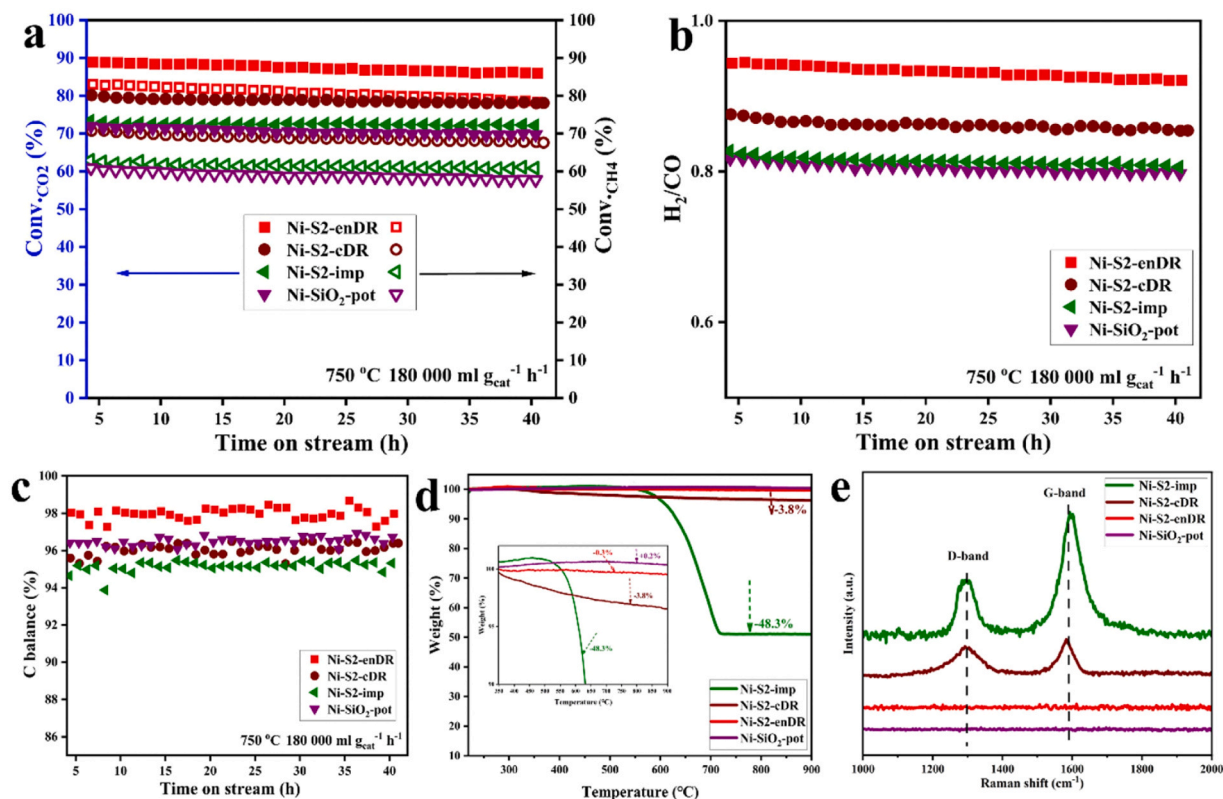
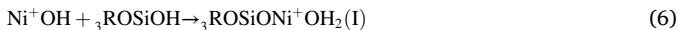
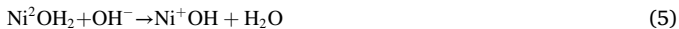


Fig. 6. Long-term durability tests at 750 °C and in GHSV = 180 L g_{cat}⁻¹ h⁻¹ a) The CO₂ and CH₄ conversion; b) The ratio of product H₂ and CO; and c) The C balance of different samples. d) TG profiles and e) Raman spectra of the spent catalysts for long-term durability tests.

3. Results and discussion

3.1. Textural characterization of the prepared catalysts

We utilized S2 as a sacrificial support and added TBAOH for dissolution. Additionally, we added EN to improve Ni²⁺ dispersion and increase the pH value in the solution, and to form the grafted Ni(II) intermediates via enhancing the degree of Ni-O-Si copolymerization (I and II) caused by the successive copolymerization reaction, as shown in formulas (1)-(4) [37]. The details will be mentioned in the discussion Section 3.5. During the recrystallization, silica tetrahedra of S2 zeolite regrow near the nickel nucleus (called nucleation growth [38,39]), and form silica nanowires bound to the Ni NPs. TEM images taken during the synthesis are shown in Supporting Information (Fig. S1).



N₂ adsorption-desorption experiments were performed for all the prepared catalysts as well as the S2 support. Different isothermal adsorption-desorption curves were obtained (Fig. 1a and b): the S2 support and Ni-S2-imp catalyst exhibited a typical type-I isotherm (Fig. 1a). This indicated that the homemade S2 support had a regular microporous structure, moreover, the Ni impregnation did not destroy its microporous structure, in line with previous reports [40]. Instead, the Ni-S2-enDR, Ni-S2-cDR, and Ni-SiO₂-pot catalysts exhibited the type-IV isotherm (Fig. 1b), with H3/H4 hysteresis loops as suggested by the International Union of Pure and Applied Chemistry (IUPAC). The Ni-SiO₂-pot catalyst exhibited relatively low adsorption in the

low-pressure region, indicating that its microporous structure was minimal. The one-pot method did not form S2 with a regular microporous structure because the addition of high-loading nickel disrupted the crystallization conditions of S2 [29,30]. Differently, both Ni-S2-enDR and Ni-S2-cDR catalysts showed a specific amount of adsorption in the low-pressure area, suggesting the presence of S2 microporous structures. Compared to the Ni-S2-enDR catalyst, the Ni-S2-cDR catalyst had a smaller adsorbed quantity in the high-pressure region. This might indicate that the Ni-S2-cDR catalyst primarily consisted of narrow pores formed by layered structures [34,41]. Their pore size distribution curves also proved that the S2 and Ni-S2-imp were microporous structure, and the Ni-SiO₂-pot was mesoporous structure, while the Ni-S2-cDR and Ni-S2-enDR developed a multi-level pores structure. (Fig. S2). The textural parameters of S2 and fresh catalysts were summarized and presented in Table S1. The specific area, from largest to smallest, follows S2 (468.1 m²g⁻¹) > Ni-S2-enDR (405.2 m²g⁻¹) > Ni-S2-cDR (395.4 m²g⁻¹) > Ni-S2-imp (362.8 m²g⁻¹) > Ni-SiO₂-pot (111.9 m²g⁻¹). The S2 had the largest S_{BET} because of its regular microporous structure. The S2 structure of the Ni-S2-enDR catalyst was partially disrupted, but its nanowire structure still exhibited high S_{BET}. The Ni loading in the sample was determined using XRF spectroscopy and the Ni dispersion was identified by H₂-pulse chemisorption, wherein the Ni-S2-enDR sample exhibited the highest Ni dispersion of 10.2% under the same loading of 10% (Table S1).

XRD was used to study the phase structure of the samples. As shown in the diffraction pattern of the homemade S2 (Fig. 1c), the peaks at 7.9°, 8.8°, 23.1°, 23.9°, and 45.2° consist with the features reported for S2 zeolite structure [42]. Ni-S2-imp catalyst not only showed the characteristic diffraction of S2, but also exhibited distinct NiO characteristic peaks at 37.2°, 43.3°, and 62.9°, indicating that the Ni with high loading tended to aggregate into larger particles [43]. For the Ni-SiO₂-pot catalyst, the pattern showed a wide diffraction peak between 15° < 2θ < 35°, which was attributed to the presence of amorphous silica

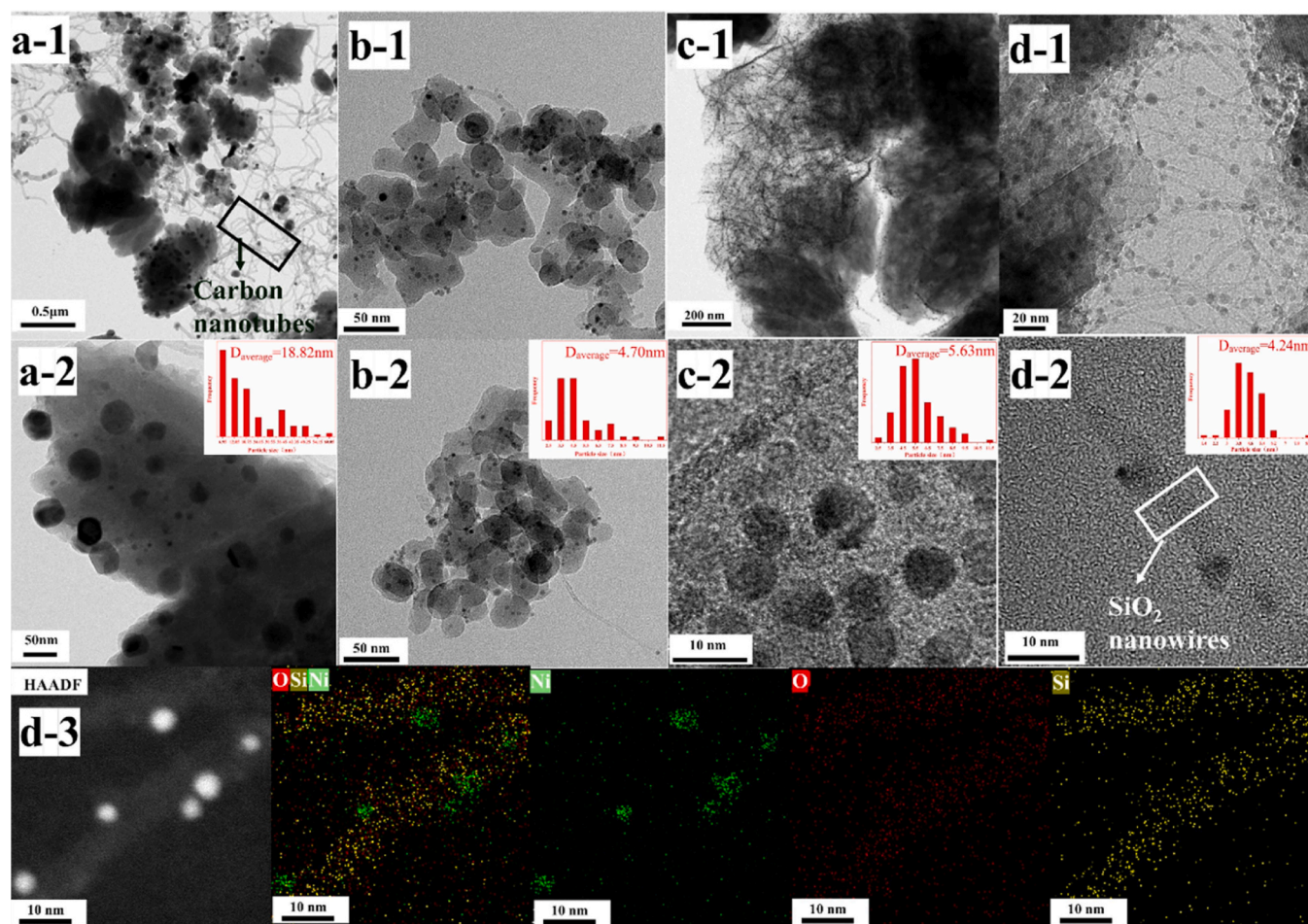


Fig. 7. The TEM image of the spent catalysts after long-term tests: a) Ni-S2-imp; b) Ni-SiO₂-pot; c) Ni-S2-cDR; d) Ni-S2-enDR. And STEM-HAADF image of the spent Ni-S2-enDR with the EDS elemental maps (O, Si, and Ni elements are labeled as red, yellow, and green, respectively).

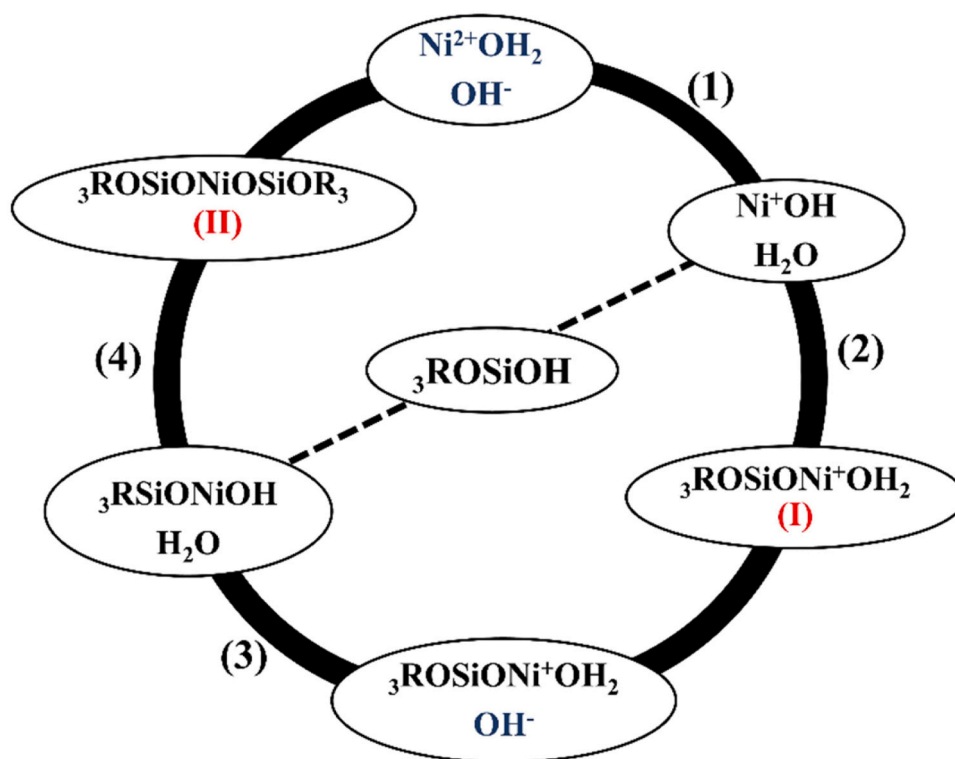
and nickel silicate structure [30,34]. For Ni-S2-cDR and Ni-S2-enDR catalysts, the patterns only showed weakly the characteristic peaks of S2. This indicated that the dissolution-recrystallization process partially destroyed the S2 structure, in line with the N₂-physisorption results that a specific amount of adsorption in the low-pressure area. However, the catalyst retained still some S2 structures. This might be one of the reasons for the stability of the Ni-S2-enDR catalyst during the DRM reaction. Furthermore, the XRD patterns of Ni-SiO₂-pot, Ni-S2-cDR, and Ni-S2-enDR catalysts did not show any diffraction peaks of NiO due to the high dispersion of Ni NPs [43]. The XRD diffraction pattern of the spent catalysts was displayed in Fig. 1d. It was shown that the diffraction peak of Ni-S2-imp shifted from 43.3° to 44.5° after the reaction, indicating the conversion of NiO into metallic Ni [44]. The diffraction patterns of the other catalysts exhibited faint peaks at 44.5°, however, almost negligible for Ni-S2-enDR. This phenomenon suggested that the Ni NPs size of the Ni-S2-enDR catalyst remained after the DRM reaction. In addition, we calculated the crystallization degree of the fresh and the spent catalysts, with reference to the intensity of S2 characteristic peaks (23.9°). Summarized in Table S1, as can be seen that the crystallinity of Ni-S2-enDR changed minimally in all catalysts after the reaction.

The catalysts before the reaction were characterized via TEM and the results are shown in Fig. 2. For the Ni-S2-imp catalyst (Fig. 2a), larger Ni NPs with an average particle size of 16.85 nm were observed and located on the outer surface of S2, also as can be seen the SEM images of S2 in Fig. S3. The Ni-SiO₂-pot catalyst (Fig. 2b) exhibited the Ni NPs size of 4.63 nm. The Ni particles were surrounded by amorphous silica, which was obtained as the high Ni content destroyed the crystallization during S2 synthesis, as suggested by XRD results. Ni NPs of 4.44 nm were

obtained for the Ni-S2-cDR catalyst (Fig. 2c), which were embedded in a layer-upon-layer sheet structure by Ni phyllosilicate. For the Ni-S2-enDR catalyst (Fig. 2d), some silica nanowires were observed on the S2 surface, which was connected with 4.25 nm Ni NPs in series. To further prove this, STEM-HAADF images with EDS elemental line-scan and maps were carried out and shown in Fig. 2e-g, the silica nanowire in transverse and longitudinal directions were partially passing through Ni NPs, demonstrating a semi-embedded structure in the Ni-S2-enDR sample.

3.2. Investigation of the metal-support interaction

To investigate the metal-support interaction of Ni-S2-enDR, Ni-S2-cDR, and Ni-S2-imp catalysts, H₂-TPR, and XPS were performed. Due to the amorphous structure of Ni-SiO₂-pot, the subsequent characterization would not be considered. First, H₂-TPR experiments of the fresh catalysts were carried out. Previous studies indicated that the reduction peak at 300–550 °C was associated with the reduction of NiO species, corresponding to weak metal-support interaction [18,45]. The reduction peak at 550–750 °C generally corresponds to the reduction of the nickel silicate, which was ascribed to the strong metal-support interaction through Ni-O-Si copolymerization [18,34,46]. As the degree of Ni-O-Si copolymerization increased, the temperature of reduction also increased from 550 °C to 750 °C. And the reduction peak at 550–650 °C, and > 710 °C corresponded to a 1:1 and 2:1 nickel phyllosilicate species (Ni PS), respectively [46–48]. In this work, the Ni-S2-imp catalyst was mainly characterized by the reduction peak of NiO (the fitted green peaks of Fig. 3a), suggesting the presence of weak metal-support



Scheme 1. Schematic diagram of the successive copolymerization reactions (1)-(4) in the solution.

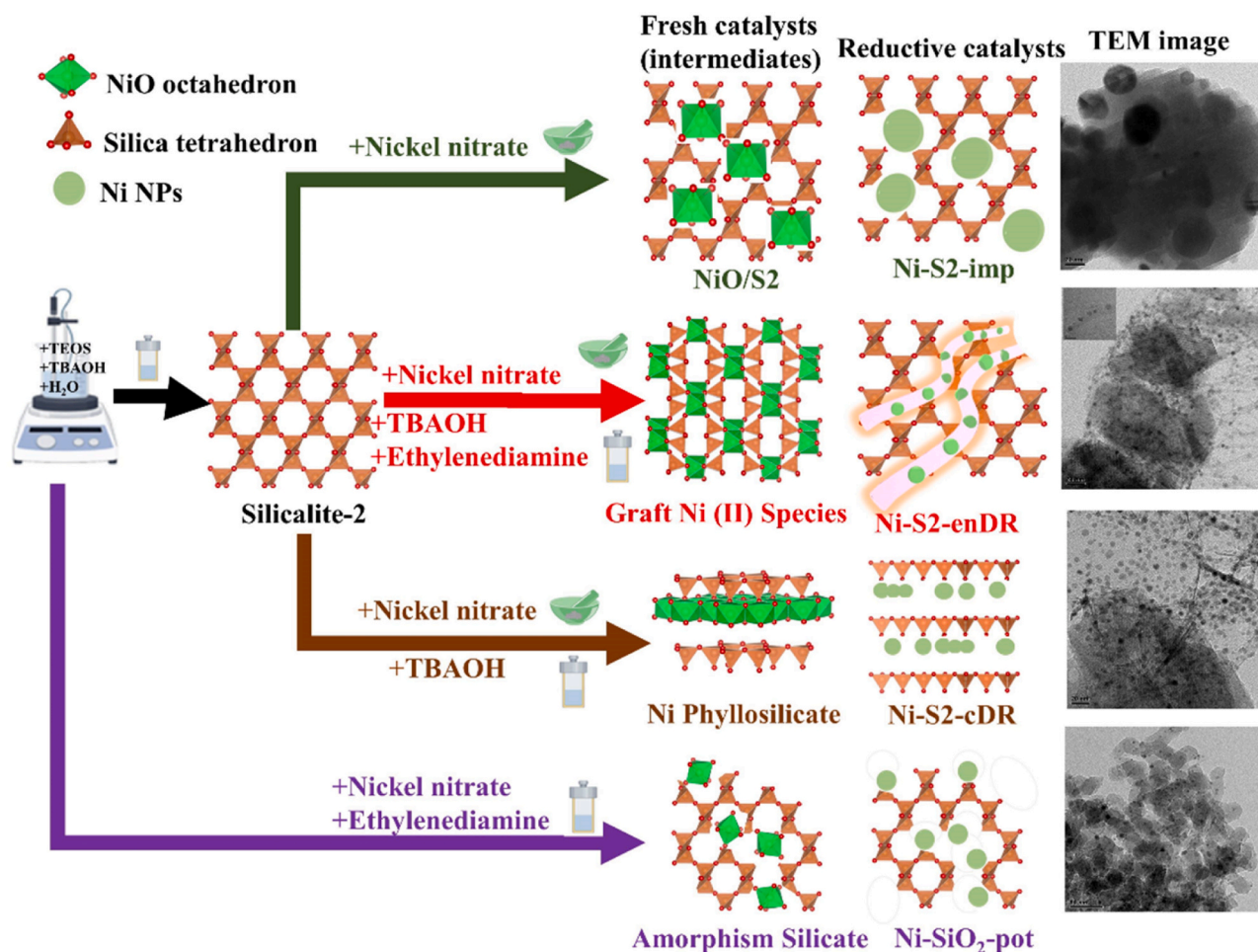
interaction. Both the Ni-S2-cDR and Ni-S2-enDR catalysts exhibited two hydrogen consumption peaks. The Ni-S2-cDR catalyst exhibited more reducible NiO species ($<550\text{ }^{\circ}\text{C}$), as well as a lower temperature of $640\text{ }^{\circ}\text{C}$ for the main reduction peak, compared to Ni-S2-enDR ($690\text{ }^{\circ}\text{C}$). This indicates a higher level of Ni-O-Si copolymerization during the synthesis of the Ni-S2-enDR catalyst.

The chemical state and distribution of the Ni species were analyzed using XPS. As shown in Fig. 3b, the Ni 2p binding energy in the range of 853–859 eV corresponds to the oxidation state of Ni^{2+} [49]. It was reported that NiO species typically showed a double peak shape, with a double peak value between 853 eV and 855 eV, while nickel silicate species could reach 856 eV to 859 eV [50]. In between, the region of 856–857 eV (Ni-O-Si 1) could be ascribed to the excitation of photoelectrons in 1:1 type Ni PS ($\text{Ni}_3\text{Si}_2\text{O}_6\text{H}_4$) or Ni_2SiO_4 species [45,49], while 857–859 eV (Ni-O-Si 2) could be the excitation of photoelectrons in 2:1 type Ni PS ($\text{Ni}_3\text{Si}_4\text{O}_{11}\text{H}_2$) or grafted Ni(II) species [51–54]. Through successive reactions that formed different degrees of Ni-O-Si copolymerization (I or II in formulas (1)–(4)), the metal-support interaction of the catalyst was reinforced, increasing the Ni 2p binding energy. It could be observed that the Ni 2p binding energy for the three catalysts follows: Ni-S2-imp $<$ Ni-S2-cDR $<$ Ni-S2-enDR. Furthermore, the corresponding Si 2p binding energy for the three catalysts showed an opposite trend: Ni-S2-enDR $<$ Ni-S2-cDR $<$ Ni-S2-imp (Fig. S4), due to the higher Ni-O-Si copolymerization on the surface of the fresh Ni-S2-enDR catalyst [18], in line with the H_2 -TPR results. By deconvolution, we calculated the proportions of different nickel species on the near-surface region based on the fitted peaks. As shown in Table 1, the nickel species of the Ni-S2-imp catalyst surface were dominated by NiO species (58.93%, green series in Fig. 3b) with lower peaks. The Ni-S2-cDR catalyst exhibited 89.94% of nickel silicate species, including 61.98% Ni-O-Si 1 and 27.96% Ni-O-Si 2. In comparison, a higher Ni-O-Si 2 ratio of 40.21% was observed for the Ni-S2-enDR catalyst, which could be due to the presence of grafted Ni(II) species with a stronger degree of Ni-O-Si copolymerization.

3.3. Investigation of the Ni-O-Si copolymerization

To further investigate the nickel silicate species in the bulk phase of catalysts, we employed spectral analysis including UV-vis, FTIR spectra, and EXAFS analysis. As shown in Fig. 4a, the UV-vis spectra of fresh catalysts confirmed the degree of Ni-O-Si interaction. The fresh catalysts exhibited completely different absorbance before and after 233 nm (Fig. 4a). The absorbance was around 218 nm due to the charge transfer of $\text{O}^{2-} \rightarrow \text{Ni}^{2+}$ in the Ni-O-Si [17,55]. The absorbance followed the trend: Ni-S2-enDR $>$ Ni-S2-cDR $>$ Ni-S2-imp, shows more the bond of Ni-O-Si presented over Ni-S2-enDR. The broad absorption band in 240–320 nm was characteristic of the charge transfer transition of $\text{O}^{2-} \rightarrow \text{Ni}^{2+}$ in the NiO octahedral clusters [56]. With higher absorbance, the Ni-S2-imp exhibited more NiO clusters while barely presented on the Ni-S2-enDR, in line with XRD results (Fig. 1c). Note that Ni-S2-enDR exhibited the distinct absorption at 410, and 660 nm (Fig. 4a), which could be attributed to isolated hexacoordinated grafted Ni (II) species [53].

As shown from the FTIR spectra in Fig. 4b, some bands were observed between 400 and 1400 cm^{-1} , which confirms the presence of S2 support [30]. All samples exhibited vibration bands at 446, 805, and 1087 cm^{-1} , and could be ascribed to the O-Si-O bending mode, the symmetric and asymmetric stretching vibrations, respectively [45]. The vibration bands at 560 cm^{-1} indicated the presence of a double 5-ring (D5R) in the pentasil structure of S2 [30]. A 2:1 nickel phyllosilicate characteristic band were easily discernible in Ni-S2-cDR with the doublet at 670 and 710 cm^{-1} (Fig. 4b) [45,56]. It should be mentioned that only the Ni-O-Si sample exhibited a band at 1035 cm^{-1} , corresponding to the asymmetrical stretching vibration of the Ni-O-Si [17, 57]. This indicates the Ni-O-Si content was too low to be observed on both Ni-S2-cDR and Ni-S2-imp, while the Ni-S2-enDR exhibited the strongest Ni-O-Si interaction even with the same Ni loading. Note that the stretching vibration of the surface Si-OH bond at 974 cm^{-1} in the Ni-S2-imp sample, exhibited a higher intensity compared to the other two samples [58]. Because Ni modified the Si-OH group on the surface



Scheme 2. Schematic diagram of the four simple preparation strategies (green part is Ni-S2-imp; red part is Ni-S2-enDR; brown part is Ni-S2-cDR; purple part is Ni-SiO₂-pot).

by attaching to the silanol group for Ni-S2-cDR and Ni-S2-enDR catalysts [45]. This point will be further discussed in detail in the coming sections.

As shown in Fig. 4c, the X-ray absorption near-edge spectra (XANES) of Ni K-edge for the fresh and reduced catalysts showed a clear difference in line shape and position. At the pre-edge of the XANES, the location of normalized adsorption peak of the fresh catalysts was similar to that of the NiO reference (8333.9 eV), attributed to $1s \rightarrow 3d$ electronic transition of Ni²⁺ [17]. In contrast, the XANES of the reduced catalysts was similar to that of Ni reference, attributed to the electronic transition of Ni⁰. However, the XANES of the reduced Ni-S2-enDR still revealed that partial NiO or α -Ni(OH)₂ feature (Fig. 4c). At the main-edge of the XANES, the normalized adsorption value of the reduced Ni-S2-enDR was higher than that of the other reduced catalysts and the Ni foil reference, indicating that the reduced Ni-S2-enDR still exhibited the metal-support interactions (Ni-O-Si) [18,21]. The Ni K-edge EXAFS of the reduced catalysts in the *R*-space are displayed in Fig. 4d. All catalysts exhibited a peak at 2.48 Å, which was identical to that of Ni foil [59]. A positive relationship was reported between the intensity of this peak and the size of Ni NPs [18]. In this work, the average size of Ni NPs in the catalyst decreased in the order indicated by Fig. 4d: Ni-S2-imp > Ni-S2-cDR > Ni-S2-enDR, consistent with the TEM results (Fig. 2).

Fig. 4e-f depicts the EXAFS of the Ni K-edge for the fresh catalysts and standard samples in *k*- and *R*-space, respectively. As shown in Fig. 4g-i, the curve-fitted figures of the fresh catalysts, and the fitted results are presented in Table 2. (The fitted details of standard samples

are presented in Table S2 and Figs. S5–6).

First, there was a peak at 2.07 Å for the fresh catalysts and the NiO standard sample (Fig. 4f), which could be considered as the first shell (1st O backscatter) of the absorbed Ni atom. Among them, the coordination number (CN) obtained from the 1st O backscatter in the fresh catalysts (Table 2) and the NiO standard samples (Table S2) were approximately 6.5. This could infer that the 1st O backscatter was a NiO₆ octahedron [60]. Then, we observed a noticeable distinction in the second shell (2nd backscatter) of the fresh catalysts (Fig. 4f). The 2nd Ni backscatter peak of the Ni-S2-imp matched the standard sample for NiO, indicating that NiO was present in the Ni-S2-imp sample, in line with the XPS results. However, the 2nd backscatter peak of the Ni-S2-cDR and Ni-S2-enDR samples were shifted to a higher distance compared to NiO, which was closer to the second shell of the α -Ni(OH)₂ standard sample (Fig. 4f). This indicated that nickel silicate was the intermediate formed in the Ni-S2-cDR and Ni-S2-enDR catalysts [60]. More specifically, As shown in Fig. 4f, the intensity of the second shell peak of the Ni-S2-enDR was slightly lower and shifted to a higher *R* compared to Ni-S2-cDR. According to the fitted data (Table 2), the 2nd Ni and Si backscatter of the Ni-S2-cDR catalyst consisted of 5.2 Ni atoms and 4.4 Si atoms. This corresponded to a Si to Ni ratio of 0.85, which was close to the ratio of Ni PS (< 1), the *R*_{Ni-Ni} was 3.02 Å, and the *R*_{Ni-Si} was 3.27 Å [53]. Thus, the nickel silicate species in the bulk phase of the Ni-S2-cDR catalyst were mainly Ni PS (1:1 type or 2:1 type). However, the 2nd Ni and Si backscatter of the Ni-S2-enDR catalyst comprised 2.9 Ni atoms and 6.6 Si atoms, and the ratio of Si to Ni was 2.28, which was similar to the ratio of grafted Ni(II) species (2.2 > 1) [54]. The *R*_{Ni-Ni} was 3.07 Å, while the *R*

Ni-Si was 3.25 Å (Table 2). Hence, the main nickel silicate species observed in the bulk phase of the Ni-S2-enDR catalyst were primarily grafted Ni(II) species. The nickel species in the bulk phase of the Ni-S2-imp catalyst only consisted of the 2nd Ni backscatter of NiO. This backscatter was composed of 15.1 Ni atoms and did not contain any Si atoms. In conclusion, as more Si was gathered around an octahedral coordination of Ni, the Si: Ni ratio increased. The order of the Si: Ni atoms of adsorbed Ni atom for intermediates, from smallest to largest was as follows: Ni-S2-imp (NiO) < Ni-S2-cDR (Ni PS) < Ni-S2-enDR (grafted Ni(II) species). This order determined the degree of Ni-O-Si copolymerization, thereby resulting in the different metal-support interactions, consistent with UV-vis and FTIR spectra results.

3.4. DRM performance of the catalysts

As shown in Fig. 5a-b, both CH_4 and CO_2 conversions of the investigated catalysts increased with increasing temperature, and the ratio of product H_2 and CO as shown in Fig. S7, in line with the thermodynamic predictions [61]. Compared to other catalysts, the Ni-S2-enDR catalyst exhibited a higher DRM activity, with almost full CO_2 conversion achieved at 800 °C, and approximately 28% at 500 °C. This was close to the equilibrium conversion (atmospheric pressure, CH_4 : CO_2 : N_2 = 1:1:2) at the corresponding temperature. The excellent activity could be attributed to the high dispersion of the active site on its nanowire structure, resulting in enhanced CH_4 decomposition and CO_2 adsorption, while the presence of multiple pores in the S2 support enhanced the diffusion of reactants. The initial CO_2 conversion of the Ni-S2-imp catalyst was approximately 45% at 650 °C, however, obvious carbon accumulation was observed after 2 h, preventing the further proceeding of the test. This could be explained by the formation of large Ni NPs with the test proceeding, as the aggregation of C* became easier on the large Ni NPs [12–16]. Moreover, catalysts were exposed to a condition where carbon formation is thermodynamically favorable. At 650 °C, the Ni-S2-enDR exhibited the best catalytic performance for the reactant's conversion and product ratio H_2/CO . The spent Ni-S2-enDR showed negligible coke deposition in the TG tests (Fig. S8). As shown in Fig. 5c-d, the CO_2 and CH_4 conversion steadily decreased a little for Ni-S2-enDR from 180k, 300–450k $\text{ml g}_{\text{cat}}^{-1} \text{h}^{-1}$. The high and stable catalytic performance in 30 h indicated that the Ni-S2-enDR was highly resistant to carbon deposition even with a high GHSV of 450k $\text{ml g}_{\text{cat}}^{-1} \text{h}^{-1}$. In comparison, relatively unstable conversions were observed for other samples (Fig. 5e-f). This was due to the increased instability of nickel active sites at high GHSV.

As shown in Fig. 6a, the CO_2 conversion of the Ni-S2-enDR catalyst remained around 90%, and the CH_4 conversion (80%) with stable catalytic performance in 40 h. Meanwhile, hardly any morphology change was observed for the Ni-S2-enDR catalyst after the reaction, as shown in the TEM image (Fig. 7) and XRD pattern (Fig. 2d). For the H_2/CO product (Fig. 6b), the Ni-S2-enDR catalyst exhibited the highest ratio (0.95), indicating that the lowest degree of the reverse water-gas shift reaction (RWGS) occurred in the DRM reaction [10]. Additionally, the C balance of different catalysts showed more than 94% (Fig. 6c). Due to the effect of the different carbon deposition on the catalysts, the Ni-S2-enDR catalysts revealed a higher C balance (98%) during the DRM test [17,21]. Fig. 6d shows the TG curves of the catalysts after the DRM test at 750 °C for 40 h. The Ni-S2-imp catalyst exhibited a 48% weight loss. This suggests that the Ni-S2-imp catalyst experienced significant carbon deposition during the DRM reaction [62]. In comparison, the Ni-S2-cDR catalyst showed a carbon deposition of 3.8%, while hardly any weight loss could be observed for the Ni-S2-enDR catalyst (0.3%). This could be attributed to the dual confinement of nickel, including the strong metal-support interaction (chemically) and silica nanowire structure encapsulation (physically). As displayed in Fig. 6e, Raman spectra were used to identify the crystalline order of carbon over spent catalysts. The Ni-S2-imp and Ni-S2-cDR catalysts show two main peaks of carbonaceous at approximately D band of 1335 cm^{-1} and G band of 1586 cm^{-1} [17,18]. It was reported that the higher the ratio of I_G to I_D ,

the more graphitic carbon was formed [63]. Hence, the graphitization degree of carbon deposition on Ni-S2-imp was higher. The Ni-S2-enDR and Ni-SiO₂-pot hardly appeared signal of D band or G band, in line with the TG results (Fig. 6d).

As shown in Fig. 7a-d, numerous carbon compounds were formed on the spent Ni-S2-imp catalyst with the size of Ni NPs increased from 16.85 to 18.82 nm [63]. The Ni NPs were larger both on the spent Ni-S2-cDR and the spent Ni-SiO₂-pot catalyst. However, no growth in Ni NPs size was observed over the spent Ni-S2-enDR catalyst (4.24 nm). Moreover, STEM-HAADF images with EDS elemental maps were carried out and shown in Fig. d-3, the nanowires of the Ni-S2-enDR catalyst were SiO₂ instead of carbon nanotubes [63].

3.5. Discussion

In this work, the Ni-silicalite-2 catalyst with a SiO₂ nanowires was first synthesized by the EN-assisted dissolution-recrystallization method. Scheme 1 depicts the successive copolymerization reactions (1)-(4) mentioned above. As can be seen, the reaction between hydroxyl Ni (Ni^+OH or NiOH species) and hydroxyl Si ($\text{Si}(\text{OH})_3$ species) played a decisive role in forming Ni-O-Si copolymerization during the solution step of the catalyst preparation method [64,65]. Furthermore, the hydroxy Ni is formed through the reaction of Ni^{2+} and OH^- in the solution, which is influenced by the presence of octahedral Ni^{2+} dispersed in aqueous solution ($\text{Ni}^{2+}\text{OH}_2$), and the pH value of the solution, as indicated by the formulas (1) and (3). During this process (Scheme 2, red line), Ni^{2+} was more evenly distributed and the content of $\text{Ni}^{2+}\text{OH}_2$ species increased due to the formation of complex $[\text{Ni}(\text{en})_3]^{2+}$, meanwhile, the high alkalinity of EN also increased the pH value of the solution, thereby producing more hydroxy Ni [53,54]. In addition, the $\text{Si}(\text{OH})_3$ species is silica tetrahedrons containing hydroxyl in the solution. On one hand, when the -R group was Ni^{2+} octahedrons, the silica tetrahedron and Ni^{2+} octahedron were connected by the Ni-O-Si, as shown in formulas (2) or (4). In other words, the nickel silicate with different copolymerization degrees connected by the Ni-O-Si was formed. On the other hand, when the -R group was polymerized another $\text{Si}(\text{OH})_3$ species, the zeolite with crystal structure or the amorphous silica was formed by the connection of the Si-O-Si [28].

Therefore, it is important to figure out the -R group a silica tetrahedron (Si-O-Si) or a Ni^{2+} octahedron (Ni-O-Si), as well as the degree of their copolymerization. To do so, different reference catalysts, prepared by one-pot, impregnation, and conventional dissolution-recrystallization methods, were used for comparison. For the Ni-SiO₂-pot catalyst (Scheme 2, purple line), although the addition of EN in the solution increased the content of hydroxy Ni, the presence of organic silicon source TEOS and template TBAOH led to more hydroxy Si, so most hydroxy Si would polymerize rather than copolymerize with hydroxy Ni. In addition, the presence of hydroxy Ni disrupted the crystallization environment of S2, resulting in the formation of most the amorphous silica. In the impregnation process (Scheme 2, green line), the surface of the S2 had only a few hydroxy Si and hydroxy Ni, forming a weak metal-support interaction. Thus, most of the Ni NPs easily migrated on the surface to form large sizes of Ni NPs after reduction. During the dissolution-recrystallization process, the hydroxy Si formation involved the dissolution of silica, which depended on the pH of the solution and the S_{BET} [66,67]. For the Ni-S2-enDR catalysts (Scheme 2, red line), S2 with a high S_{BET} was used as a sacrificial support and was dissolved by TBAOH, resulting in the production of more hydroxy Si. At the same time, the addition of EN produced a large amount of hydroxyl Ni. Therefore, hydroxy Si would copolymerize with hydroxy Ni to form grafted Ni (II) intermediates and nucleate around it to form a silica nanowire, with highly dispersed Ni NPs (Fig. 2d) [38,39]. However, in the Ni-S2-cDR catalyst (Scheme 2, brown line), without the addition of EN, there was a small amount of hydroxy Ni, and more Ni^{2+} in the solution would gather together. Therefore, hydroxy Si would copolymerize with hydroxy Ni to form Ni PS intermediates. And hydroxy Si

around it polymerized to form a silica lamellar structure [38,39]. Thus, there was a competition of concentration between the hydroxy Ni and the hydroxy Si in the solution. In particular, the coordination number ratio of Si to Ni atoms of absorbed nickel atoms was 2.2, which could form grafted Ni(II) species with strong metal-support interaction based on EXAFS and other characterization results.

4. Conclusion

In this work, we reported a novel Ni-silicalite-2 catalyst with nanowires synthesized by adding EN in the dissolution-recrystallization process. The H₂-TPR, XPS, UV-vis, and FTIR results demonstrated that the successive copolymerization reaction generated intermediates with an elevated Ni-O-Si copolymerization level thanks to the increase of hydroxy Ni content in comparison to nickel phyllosilicate. Moreover, the coordination number ratio of Si to Ni was 2.28 in the 2nd backscatter of the adsorbed Ni atoms, proving the formation of grafted Ni(II) intermediates. Figurative, the S2 framework was shattered into a silica nanowire, while Ni was dispersed and firmly affixed by EN into nanowire space. As a result, the Ni-S2-enDR catalysts displayed excellent Ni NPs dispersion and confinement effect at a high Ni loading of 10 wt%. At 800 °C and 180 L g_{cat}⁻¹ h⁻¹, almost full CO₂ conversion was achieved in the DRM reaction, demonstrating the highest catalytic activity and stability of Ni NPs relative to the other three catalysts. This work provides a novel catalyst preparation strategy as well as new insights into the atom-level understanding of nickel-silicon coordination for the future development of highly active and stable reforming catalysts.

CRediT authorship contribution statement

Hongyu Li: Visualization. **Bingrong Pan:** Methodology. **Wenbo Kong:** Software. **Yuhan Sun:** Funding acquisition, Conceptualization. **Jun Zhang:** Investigation, Funding acquisition. **Jiong Li:** Project administration, Methodology. **Lei Zheng:** Writing – review & editing. **Yu Fu:** Writing – review & editing. **Shuqing Li:** Writing – review & editing, Conceptualization. **Yidan Zhang:** Writing – original draft, Data curation.

Declaration of Competing Interest

The authors declare no competing financial interest.

Data availability

The data that support the findings of this study are available from the corresponding author upon request.

Acknowledgements

We acknowledge the support from the National Key R&D Program of China (grant numbers 2022YFA1504701& 2022YFA1504704& 2023YFB4005202& 2023YFB4005205) the National Natural Science Foundation of China (grant numbers 22378414), and the Youth Innovation Promotion Association CAS (grant numbers 2022287). We thank Jupeng Bio (HK) Inc., Gaolu Air Products and Chemicals (Shanghai) Energy Technology Co., Ltd, the BL11B beamline of Shanghai Synchrotron Radiation Facility, and Shanghai Functional Platform for Innovation Low Carbon Technology.

Appendix A. Supporting information

Supplementary data associated with this article can be found in the online version at doi:10.1016/j.apcatb.2024.123903.

References

- [1] R. Willis, Taming the Climate? Corpus analysis of politicians' speech on climate change, *Environ. Polit.* 26 (2) (2017) 212–231.
- [2] B. Lan, K. Dong, L. Li, Y. Lei, S. Wu, E. Hua, R. Sun, CO₂ emission reduction pathways of iron and steel industry in Shandong based on CO₂ emission equity and efficiency, *Resour. Policy* 81 (2023) 103406.
- [3] B. Wang, Low-carbon transformation planning of China's power energy system under the goal of carbon neutrality, *Environ. Sci. Pollut. Res.* 30 (2023) 44367–44377.
- [4] Q. Zeng, Z. Wang, L. Liu, J. Ye, B.J. McPherson, J.D. McLennan, Modeling CH₄ displacement by CO₂ in deformed coalbeds during enhanced coalbed methane recovery, *Energy Fuels* 32 (2) (2018) 1942–1955.
- [5] F. Xu, W. Hou, X. Xiong, B. Xu, P. Wu, H. Wang, F. Kun, Y.U.N. Jian, L.I. Shuguang, Z. Lei, Y.A.N. Xia, F. Huijun, L.U. Qian, M.A.O. Delei, The status and development strategy of coalbed methane industry in China, *Petrol. Explor. Dev.* 50 (4) (2023) 765–783.
- [6] M. Bradford, M. Vannice, CO₂ Reforming of CH₄, *Catal. Rev.* 41 (1) (1999) 1–42.
- [7] M. Mahyuddin-Haris, A. Staykov, Y. Shiota, K. Yoshizawa, Direct conversion of methane to methanol by metal-exchanged ZSM-5 zeolite (Metal = Fe, Co, Ni, Cu), *ACS Catal.* 6 (12) (2016) 8321–8331.
- [8] D. Liang, Y. Wang, M. Chen, X. Xie, C. Li, J. Wang, L. Yuan, Dry reforming of methane for syngas production over attapulgite-derived MFI zeolite encapsulated bimetallic Ni-Co catalysts, *Appl. Catal., B* 322 (2022) 122088.
- [9] Y.-X. Yu, J. Yang, K.-K. Zhu, Z.-J. Sui, D. Chen, Y.-A. Zhu, X.-G. Zhou, High-throughput screening of alloy catalysts for dry methane reforming, *ACS Catal.* 11 (14) (2021) 8881–8894.
- [10] D. Pakhare, J. Spivey, A review of dry (CO₂) reforming of methane over noble metal catalysts, *Chem. Soc. Rev.* 43 (22) (2014) 7813–7837.
- [11] S. Wang, G. Max, G. Millar, Carbon dioxide reforming of methane to produce synthesis gas over metal-supported catalysts: state of the art, *Energy Fuels* 10 (4) (1996) 896–904.
- [12] F. Abild-Pedersen, J. Nørskov, J. Rostrup-Nielsen, J. Sehested, S. Helveg, Mechanisms for catalytic carbon nanofiber growth studied by ab initio density functional theory calculations, *Phys. Rev. B Condens. Matter Mater. Phys.* 73 (11) (2006), 115419.1–115419.13.
- [13] D.-L. Trimm, The formation and removal of coke from nickel catalyst, *Catal. Rev.* 16 (1) (1977) 155–189.
- [14] H.S. Bengaard, J.K. Nørskov, J. Sehested, B.S. Clausen, L.P. Nielsen, A. M. Molenbroek, J.R. Rostrup-Nielsen, Steam reforming and graphite formation on Ni catalysts, *J. Catal.* 209 (2002) 365–384.
- [15] A. Al-Fatih, A. Ibrahim, A. Fakeeha, M. Soliman, M. Siddiqui, A. Abasaeed, Coke formation during CO₂ reforming of CH₄ over alumina-supported nickel catalysts, *Appl. Catal., A* 364 (1) (2009) 150–155.
- [16] X. Wang, Y. Liu, K. Liu, J. Zhang, J. Wei, Phosphorus-tuned nickel as high coke-resistant catalyst with high reforming activity, *Int. J. Hydrog. Energy* 45 (2020) 28325–28336.
- [17] Y. Liu, Y. Chen, Z. Gao, X. Zhang, L. Zhang, M. Wang, B. Chen, Y. Diao, Y. Li, D. Xiao, X. Wang, D. Ma, C. Shi, Embedding high loading and uniform Ni nanoparticles into silicalite-1 zeolite for dry reforming of methane, *Appl. Catal., B* 307 (2022) 121202.
- [18] J. Wang, Y. Fu, W. Kong, F. Jin, J. Bai, J. Zhang, Y. Sun, Design of a carbon-resistant Ni@S-2 reforming catalyst: controllable Ni nanoparticles sandwiched in a peasecod-like structure, *Appl. Catal., B* 282 (2020) 119546.
- [19] Z.-Y. Lim, J. Tu, Y. Xu, B. Chen, Ni@ZrO₂ yolk-shell catalyst for CO₂ methane reforming: effect of Ni@SiO₂ size as the hard-template, *J. Colloid Interface Sci.* 590 (2021) 641–651.
- [20] S. Corthals, J. Nederkassel, J. Geboers, H. De Winne, J. Van Noyen, B. Moens, B. Sels, P. Jacobs, Influence of composition of MgAl₂O₄ supported NiCeO₂ZrO₂ catalysts on coke formation and catalyst stability for dry reforming of methane, *Catal. Today* 138 (1) (2008) 28–32.
- [21] W. Kong, Y. Fu, L. Shi, S. Li, E. Vovk, X. Zhou, R. Si, B. Pan, C. Yuan, S. Li, F. Cai, H. Zhu, J. Zhang, Y. Yang, Y. Sun, Nickel nanoparticles with interfacial confinement mimic noble metal catalyst in methane dry reforming, *Appl. Catal., B* 285 (2020) 119837.
- [22] M.E. Rivas, J.L.G. Fierro, M.R. Goldwasser, E. Pietri, M.J. Pérez-Zurita, A. Griboval-Constant, G. Leclercq, Structural features and performance of LaNi_{1-x}Rh_xO₃ system for the dry reforming of methane, *Appl. Catal., A* 344 (1) (2008) 10–19.
- [23] Y. Sun, R. Li, C. Song, H. Zhang, Y. Cheng, A. Nie, H. Li, D.D. Dionysiou, J. Qian, B. Pan, Origin of the improved reactivity of MoS₂ single crystal by confining lattice Fe atom in peroxymonosulfate-based Fenton-like reaction, *Appl. Catal., B* 298 (2021) 120537.
- [24] H. Wang, L. Wang, D. Lin, X. Feng, Y. Niu, B. Zhang, F.-S. Xiao, Strong metal-support interactions on gold nanoparticle catalysts achieved through Le Chatelier's principle, *Nat. Catal.* 4 (2021) 418–424.
- [25] K. Tomishige, Y. Himeno, Y. Matsuo, Y. Yoshinaga, K. Fujimoto, Catalytic performance and carbon deposition behavior of a NiO-MgO solid solution in methane reforming with carbon dioxide under pressurized conditions, *Ind. Eng. Chem. Res.* 39 (6) (2000) 1891–1897.
- [26] D. San-José-Alonso, J. Juan-Juan, M.J. Illán-Gómez, M.C. Román-Martínez, Ni, Co and bimetallic Ni-Co catalysts for the dry reforming of methane, *Appl. Catal., A* 371 (1) (2009) 54–59.
- [27] K. Kim, J. Lee, H. Lee, W. Noh, E.H. Kim, E.C. Ra, S.K. Kim, K. An, J.S. Lee, Layered double hydroxide-derived intermetallic Ni₃GaCo_{0.25} catalysts for dry reforming of methane, *ACS Catal.* 11 (17) (2021) 11091–11102.

- [28] J. Dong, J. Zou, Y. Long, Synthesis and characterization of colloidal TBA-silicalite-2, *Microporous Mesoporous Mater.* 57 (1) (2003) 9–19.
- [29] G. Vitale, H. Molero, E. Hernandez, S. Aquino, V. Birss, P. Pereira-Almao, One-pot preparation and characterization of bifunctional Ni-containing ZSM-5 catalysts, *Appl. Catal., A* 452 (2013) 75–87.
- [30] Y. Lu, D. Guo, Y. Zhao, P.S. Moyo, Y. Zhao, S. Wang, X. Ma, Confined high dispersion of Ni nanoparticles derived from nickel phyllosilicate structure in silicalite-2 shell for dry reforming of methane with enhanced performance, *Microporous Mesoporous Mater.* 313 (2021) 110842.
- [31] H. Xu, P. Wu, New progress in zeolite synthesis and catalysis, *Natl. Sci. Rev.* 9 (9) (2022) nwac045.
- [32] M. Król, Natural vs. Synthetic Zeolites, *Crystals* 10 (7) (2020) 622.
- [33] Y. Chai, W. Dai, G. Wu, N. Guan, L. Li, Confinement in a zeolite and zeolite catalysis, *Acc. Chem. Res.* 54 (13) (2021) 2894–2904.
- [34] Z. Bian, S. Kawi, Preparation, characterization and catalytic application of phyllosilicate: a review, *Catal. Today* 339 (2020) 3–23.
- [35] I.I.I. Chapter, Synthesis of High-Silica Zeolites with the Mel Type of Structure, in: P. A. Jacobs, J.A. Martens (Eds.), *Stud. Surf. Sci. Catal.*, Elsevier, 1987, pp. 147–166.
- [36] D.M. Bibby, N.B. Milestone, L.P. Aldridge, Silicalite-2, a silica analogue of the aluminosilicate zeolite ZSM-11, *Nature* 280 (5724) (1979) 664–665.
- [37] M. Kermarec, J. Carriat, P. Burattin, M. Che, A. Decarreau, FTIR identification of the supported phases produced in the preparation of silica-supported nickel catalysts, *J. Phys. Chem.* 98 (46) (1994) 12008–12017.
- [38] Q. Zhu, H. Zhou, L. Wang, L. Wang, C. Wang, H. Wang, W. Fang, M. He, Q. Wu, F.-S. Xiao, Enhanced CO₂ utilization in dry reforming of methane achieved through nickel-mediated hydrogen spillover in zeolite crystals, *Nat. Catal.* 5 (11) (2022) 1030–1037.
- [39] J. Zhang, L. Wang, B. Zhang, H. Zhao, U. Kolb, Y. Zhu, L. Liu, Y. Han, G. Wang, C. Wang, D.S. Su, B.C. Gates, F.-S. Xiao, Sinter-resistant metal nanoparticle catalysts achieved by immobilization within zeolite crystals via seed-directed growth, *Nat. Catal.* 1 (7) (2018) 540–546.
- [40] M. Wang, T. Zhao, X. Dong, M. Li, H. Wang, Effects of Ce substitution at the A-site of LaNi_{0.5}Fe_{0.5}O₃ perovskite on the enhanced catalytic activity for dry reforming of methane, *Appl. Catal., B* 224 (2018) 214–221.
- [41] Y. Zhang, H. Duan, Z. Lv, Q. Liu, X. Wu, Which is the better catalyst for CO₂ methanation-Nanotubular or supported Ni-phyllosilicate, *Int. J. Hydrog. Energy* 46 (80) (2021) 39903–39911.
- [42] X. Yan, W. Sun, L. Fan, P.-N. Duchesne, W. Wang, C. Kübel, D. Wang, S.G. H. Kumar, Y.F. Li, A. Tavasoli, T.E. Wood, D.L.H. Hung, L. Wan, L. Wang, R. Song, J. Guo, I. Gourevich, F.M. Ali, J. Lu, R. Li, B.D. Hatton, G.A. Ozin, Nickel@Siloxene catalytic nanosheets for high-performance CO₂ methanation, *Nat. Commun.* 10 (1) (2019) 2608.
- [43] C.-M. Damaskinos, M.-A. Vasiliades, A.M. Efstathiou, The effect of Ti⁴⁺ dopant in the 5 wt% Ni/Ce_{1-x}Ti_xO₂ catalyst on the carbon pathways of dry reforming of methane studied by various transient and isotopic techniques, *Appl. Catal., A* 579 (2019) 116–129.
- [44] S. Li, Y. Fu, W. Kong, B. Pan, C. Yuan, F. Cai, H. Zhu, J. Zhang, Y. Sun, Dually confined Ni nanoparticles by room-temperature degradation of AlN for dry reforming of methane, *Appl. Catal., B* 277 (2020) 118921.
- [45] T. Lehmann, T. Wolff, C. Hamel, P. Veit, B. Garke, A. Seidel-Morgenstern, Physico-chemical characterization of Ni/MCM-41 synthesized by a template ion exchange approach, *Microporous Mesoporous Mater.* 151 (2012) 113–125.
- [46] Z. Bian, S. Kawi, Highly carbon-resistant Ni-Co/SiO₂ catalysts derived from phyllosilicates for dry reforming of methane, *J. CO₂ Util.* 18 (2017) 345–352.
- [47] J. Xu, R. Xi, X. Xu, Y. Zhang, X. Feng, X. Fang, X. Wang, A₂B₂O₇ pyrochlore compounds: a category of potential materials for clean energy and environment protection catalysis, *J. Rare Earths* 38 (8) (2020) 840–849.
- [48] Y. Zhao, H. Li, H. Li, NiCo@SiO₂ core-shell catalyst with high activity and long lifetime for CO₂ conversion through DRM reaction, *Nano Energy* 45 (2018) 101–108.
- [49] A. González-Elipé, R. Alvarez, J. Holgado, J.P. Espinos, G. Munuera, J.M. Sanz, An XPS study of the Ar⁺-induced reduction of Ni²⁺ in NiO and Ni-Si oxide systems, *Appl. Surf. Sci.* 51 (1) (1991) 19–26.
- [50] R.B. Shalvoy, Characterization of coprecipitated nickel on silica methanation catalysts by X-ray photoelectron spectroscopy, *J. Catal.* 56 (3) (1979) 336–348.
- [51] P. Lorenz, J. Finster, G. Wendt, J. Salyn, ESCA investigations of some NiO/SiO₂ and NiO-Al₂O₃/SiO₂ catalysts, *J. Electron Spectrosc. Relat. Phenom.* 16 (3) (1979) 267–276.
- [52] A. S. U. Al, Activity and stability of Ni spinel catalysts in water—methane reaction, *React. Kinet. Catal. Lett.* 38 (2) (1989) 399–404.
- [53] M. Che, Z. Cheng, C. Louis, Nucleation and particle growth processes involved in the preparation of silica-supported Nickel Materials by a Two-Step Procedure, *J. Am. Chem. Soc.* 117 (1995) 2008–2018.
- [54] J. Yang, Y. Shul, C. Louis, M. Che, In situ EXAFS study of the nucleation and crystal growth of Ni particles on SiO₂ support, *Catal. Today* 44 (1) (1998) 315–325.
- [55] B. Lu, Y. Ju, T. Abe, K. Kawamoto, Grafting Ni particles onto SBA-15, and their enhanced performance for CO₂ methanation, *RSC Adv.* 5 (70) (2015) 56444–56454.
- [56] H. Chunlan, Z. Xiaoxiao, C. Bingbing, W. Xinping, A strategy of constructing the Ni@silicalite-1 catalyst structure with high activity and resistance to sintering and carbon deposition for dry reforming of methane, *Fuel* 355 (2024) 129548.
- [57] M. Kosari, S. Askari, A.M. Seayad, S. Xi, S. Kawi, A. Borgna, H.C. Zeng, Strong coke-resistance spherical hollow Ni-SiO₂-pot catalysts with shell-confined high-content ni nanoparticles for methane dry reforming with CO₂, *Appl. Catal., B* 310 (2022) 121360.
- [58] P. Kuppusamy, U. Samidurai, G. Srinivasan, S. Natarajan, Highly coke resistant Ni-Co/KCC-1 catalysts for dry reforming of methane, *Int. J. Hydrog. Energy* 48 (31) (2022) 11727–11745.
- [59] M.-A. Vasiliades, P. Djinović, A. Pintar, J. Kovač, A.M. Efstathiou, The effect of CeO₂-ZrO₂ structural differences on the origin and reactivity of carbon formed during methane dry reforming over NiCo/CeO₂-ZrO₂ catalysts studied by transient techniques, *Catal. Sci. Technol.* 7 (22) (2017) 5422–5434.
- [60] K. Ikeda, Y. Kawamura, T. Yamamoto, M. Iwamoto, Effectiveness of the template-ion exchange method for appearance of catalytic activity of Ni-MCM-41 for the ethene to propene reaction, *Catal. Commun.* 9 (1) (2008) 106–110.
- [61] W. Jang, D. Jeong, J. Shim, H. Kim, H. Roh, I.H. Son, S.J. Lee, Combined steam and carbon dioxide reforming of methane and side reactions: Thermodynamic equilibrium analysis and experimental application, *Appl. Energy* 173 (2016) 80–91.
- [62] J. Niu, Y. Wang, S.-E. Liland, S.-K. Regli, J. Yang, K.-R. Rout, J. Luo, M. Rønning, J. Ran, D. Chen, Unraveling enhanced activity, selectivity, and coke resistance of Pt–Ni bimetallic clusters in dry reforming, *ACS Catal.* 11 (4) (2021) 2398–2411.
- [63] D. Liang, Y. Wang, M. Chen, X. Xie, C. Li, J. Wang, L. Yuan, Dry reforming of methane over Mn-Ni/attapulgite: effect of Mn content on the active site distribution and catalytic performance, *Fuel* 321 (2022) 124032.
- [64] T. Mizutani, Y. Fukushima, O. Kamigaito, Mechanism of the copolymerization of silicic acid and metal ions in aqueous media, *Bull. Chem. Soc. Jpn* 63 (2) (1990) 618–619.
- [65] T. Mizutani, Y. Fukushima, A. Okada, O. Kamigaito, Synthesis of Nickel and Magnesium Phyllosilicates with 1:1 and 2:1 layer structures, *Bull. Chem. Soc. Jpn* 63 (7) (1990) 2094–2098.
- [66] G.S. Wirth, J.M. Gieskes, The initial kinetics of the dissolution of vitreous silica in aqueous media, *J. Colloid Interface Sci.* 68 (3) (1979) 492–500.
- [67] D. Dollimore, Silica chemistry, *Nature* 283 (510) (1980).